

A Probabilistic Method for Image Enhancement With Simultaneous Illumination and Reflectance Estimation

Xueyang Fu, Yinghao Liao, Delu Zeng, Yue Huang, Xiao-Ping Zhang, *Senior Member, IEEE*, and Xinghao Ding

Abstract—In this paper, a new probabilistic method for image enhancement is presented based on a simultaneous estimation of illumination and reflectance in the linear domain. We show that the linear domain model can better represent prior information for better estimation of reflectance and illumination than the logarithmic domain. A maximum *a posteriori* (MAP) formulation is employed with priors of both illumination and reflectance. To estimate illumination and reflectance effectively, an alternating direction method of multipliers is adopted to solve the MAP problem. The experimental results show the satisfactory performance of the proposed method to obtain reflectance and illumination with visually pleasing enhanced results and a promising convergence rate. Compared with other testing methods, the proposed method yields comparable or better results on both subjective and objective assessments.

Index Terms—Image enhancement, illumination, reflectance, optimization methods, maximum posterior probability (MAP).

I. INTRODUCTION

BASED on the simplification of light reflection, an observed image can be modeled as the product of the illumination and the reflectance [1]. Many methods that decompose an image into the illumination and the reflectance have been used in a series of applications, such as contrast enhancement [2]–[4], non-uniform illumination images enhancement [5], tone mapping [6]–[10], remote sensing image correction [11], image segmentation [12] and target selection and tracking [13], [14], etc.

Manuscript received December 15, 2014; revised May 13, 2015 and July 1, 2015; accepted August 25, 2015. Date of publication August 28, 2015; date of current version September 18, 2015. This work was supported in part by the National Natural Science Foundation of China under Grants 30900328, 61172179, 61103121, 81301278, 61571382 and 61571005, in part by the Fundamental Research Funds for the Central Universities under Grant 20720150169 and 20720150093, in part by the Natural Science Foundation of Fujian Province of China under Grant 2012J05160, and in part by the Research Fund for the Doctoral Program of Higher Education under Grant 20120121120043. The associate editor coordinating the review of this manuscript and approving it for publication was Prof. Jean-Francois Aujol. (*Corresponding author: Xinghao Ding*)

X. Fu, Y. Liao, D. Zeng, Y. Huang, and X. Ding are with the Fujian Key Laboratory of Sensing and Computing for Smart City, School of Information Science and Engineering, Xiamen University, Xiamen 361005, China (e-mail: fxy@stu.xmu.edu.cn; yhiao@xmu.edu.cn; dltang@xmu.edu.cn; yhuang2010@xmu.edu.cn; dxh@xmu.edu.cn).

X.-P. Zhang is with the Department of Electrical and Computer Engineering, Ryerson University, Toronto, ON M5B 2K3, Canada (e-mail: xzhang@ee.ryerson.ca).

Color versions of one or more of the figures in this paper are available online at <http://ieeexplore.ieee.org>.

Digital Object Identifier 10.1109/TIP.2015.2474701

Since computing illumination or reflectance from a single observed image is an ill-posed problem, many algorithms based on the Retinex theory [1], [15], [16] have been proposed to handle this problem. This problem is described in [17] and improved based on path computation from a random walk to a spatially opponent operation [18], [19]. Although the illumination and reflectance are decomposed, these early approaches usually bring along high computational complexity. In [20], [21], the path computation is replaced by a recursive matrix calculation to make the algorithm more efficient. However, the large number of iterations lower its efficiency. Horn proposed a mathematical alternative to the Retinex algorithm in [22], where a smoothness prior on the illumination and partial differential equation (PDE) to obtain the reflectance image are adopted. Hurlbert later defined a common mathematical foundation with some good qualities [23]. However, Hurlbert's method does not work for arbitrary scenes [2]. Other PDE-based methods model the ill-posed problem as a Poisson equation [24]–[27] and use fast Fourier transforms to generate a fast implementation. Three classical Retinex algorithms based on the center/surround Retinex include the single-scale Retinex (SSR) [3], the multi-scale Retinex (MSR) [28] and the multi-scale Retinex with color restoration (MSRCR) [2]. For these three methods, Gaussian filtering are used to estimate and remove the illumination. Although they improve the lighting, color consistency and scene restoration for digital images, they are prone to halo artifacts near edges.

The first variational interpretation of Horn's interpretation of Retinex [22] was introduced by Kimmel et al. in [29], which uses different regularization terms of illumination to establish the objective function. The illumination is estimated with this method and used for enhanced image combining with Gamma correction. Furthermore, an L2-fidelity prior between the reflectance and the observed image is introduced in [30]. This method computes both the illumination and the reflectance with Gamma correction used for further enhancement. However, the computed reflectance often loses details due to the side effect of the logarithmic transformation. This method was complemented by a non-local extension [31] to achieve an effective decomposition of illumination and reflectance. Another variational model for Retinex that unifies the previous variational models and focuses on the reflectance is proposed by Zosso et al. [32], [33]. A kernel-based Retinex variational model, which shares the same intrinsic character-

istics of the original Retinex and established in the linear domain, is introduced in [34]. An analysis of the action of this model on contrast is provided in the literature. This method can deal with color cast and enhance both under- and over-exposed images. A perception based color correction of digital images in the variational framework in the linear domain are presented in [35] and [36]. Both color enhancement and local contrast improvement can be achieved in this method. Meanwhile, a numerical implementation of the gradient descent technique is also shown in these works. The numerical approximation can be performed in $O(n \log n)$ operations, where n is the number of pixels. Recently, a Retinex approach based on a variational Bayesian method was proposed in [37]. In this literature, different distributions are used to model the reflectance, the illumination and other parameters, and then the variational Bayes approximation approach is adopted to estimate both the illumination and the reflectance. However, the computed reflectance is also over smoothed and finer details are lost due to the logarithmic transformation [37]. In addition, the computational cost is high since it requires calculations of some linear equations.

To effectively decompose illumination and reflectance from one single observed image, most of the above methods use the logarithmic transformation for pre-processing not only to reduce the computational complexity [17] but also to simulate human vision perception mechanism, such as Weber's law [38]. However, since the logarithmic transformation suppresses the variation of gradient magnitude in bright regions, solving the ill-posed problem in the logarithmic domain may lead to loss of finer structural details in these areas. Meanwhile, many existing methods solve the ill-posed problem using priors on either illumination or reflectance. In other words, different regularization terms of illumination and reflectance are not fully utilized to solve this problem.

In this paper, a novel probabilistic method for image enhancement with simultaneous illumination and reflectance estimation in the linear domain is proposed. The core concept is that formulating in the linear domain can better represent prior information for better estimation of reflectance and illumination. First, a probabilistic model for simultaneously estimating reflectance and illumination in the linear domain is introduced using a Maximum a Posteriori (MAP) formulation. Then characteristics of the logarithmic transformation are analyzed to show that estimating illumination and reflectance in the linear domain yields better performance. Finally, to decompose illumination and reflectance efficiently, the MAP problem is transformed into an energy minimization problem. An alternating direction method of multipliers (ADMM) is adopted to estimate the parts of illumination and reflectance simultaneously. The optimization algorithm is computationally efficient and the convergence is guaranteed [39].

This paper is organized as follows: the new probabilistic model for estimating reflectance and illumination is introduced in section II. Then in section III, the properties of logarithmic transformation are analyzed. Section IV gives details of the optimization strategy. Experimental results are shown in

section V. Finally the work is concluded in section VI followed by the Appendix part to explain the solution existence for the minimization problem.

II. A PROBABILISTIC MODEL FOR SIMULTANEOUS ILLUMINATION AND REFLECTANCE ESTIMATION

The physical model of light reflection can be simply described as $\mathbf{S} = \mathbf{R} \cdot \mathbf{I}$, where the vector \mathbf{S} is the observed image within the range [0, 255] in an 8-bit image, \mathbf{R} is the reflectance within the range [0, 1], \mathbf{I} is the illumination image within the range [0, 255] and “.” denotes element-wise multiplication. Since the primary goal is to estimate both illumination \mathbf{I} and reflectance \mathbf{R} from one observed image \mathbf{S} , the general physical model can be seen as a posterior distribution by Bayes' theorem,

$$p(\mathbf{I}, \mathbf{R} | \mathbf{S}) \propto p(\mathbf{S} | \mathbf{I}, \mathbf{R}) p(\mathbf{I}) p(\mathbf{R}), \quad (1)$$

where $p(\mathbf{I}, \mathbf{R} | \mathbf{S})$ is the posterior distribution, $p(\mathbf{S} | \mathbf{I}, \mathbf{R})$ is the likelihood, and $p(\mathbf{I})$ and $p(\mathbf{R})$ represent the prior probabilities on the illumination and the reflectance, respectively. To reduce the computation complexity, most methods use the logarithmic transformation to transfer multiplication into addition as a pre-processing step [17]. In addition, the logarithmic transformation enhances details in the image by improving contrast in dark regions, which is more sensitive to perceive by human eyes than bright areas according to Weber's law [38]. However, the side effect to the logarithmic transformation is that undesired structure are amplified in the low magnitude stimuli areas and edges may become fuzzy. Therefore, this characteristic of logarithmic transformation may lead to incorrect use of priors, and the reason will be elaborated in the next section. So, the proposed probabilistic model is operating in the linear domain, described as follows.

Likelihood $p(\mathbf{S} | \mathbf{I}, \mathbf{R})$: The estimated error $\mathbf{\epsilon} = \mathbf{S} - \mathbf{R} \cdot \mathbf{I}$, is assumed to be an independent and identically distributed (i.i.d.) random variable with a Gaussian distribution with zero mean and variance ζ_1^2 . The likelihood $p(\mathbf{S} | \mathbf{I}, \mathbf{R})$ is

$$p(\mathbf{S} | \mathbf{I}, \mathbf{R}) = N(\mathbf{\epsilon} | 0, \zeta_1^2 \mathbf{1}). \quad (2)$$

where $\mathbf{1}$ is the identity matrix.

Prior $p(\mathbf{R})$: Based on the well-known assumption that the reflectance contains edges and is piece-wise continuous [30], [37], the distribution of gradients of reflectance is formulated with a Laplacian distribution with location zero and scale ζ_2 :

$$p(\mathbf{R}) = L(\nabla \mathbf{R} | 0, \zeta_2 \mathbf{1}), \quad (3)$$

where ∇ is the gradient operator in both the horizontal and vertical directions.

Prior $p(\mathbf{I})$: For illumination, two components are introduced to design $p(\mathbf{I})$. One is the distribution of gradients based on the assumption that the illumination is spatially smooth [29], [30], [37]. The other is designed here as a regularization term to constrain the scale of illumination, as the illumination and the reflectance are not in the same numerical range.

To enforce spatial smoothness in the illumination, the Gaussian distribution, with zero mean and variance ζ_3^2 ,

of gradients is utilized to model the first component. Therefore the first component is written as:

$$p_1(\mathbf{I}) = N(\nabla\mathbf{I}|0, \zeta_3^2 \mathbf{I}). \quad (4)$$

For the second part of the prior, the Gaussian distribution is also adopted to avoid the scaling problem based on the white patch assumption. The second component is written as:

$$p_2(\mathbf{I}) = N(\mathbf{I}|I_0, \zeta_4^2 \mathbf{I}), \quad (5)$$

where I_0 is the mean of the Gaussian distribution and ζ_4^2 is the variance. Since the illumination does not change sharply in most cases, I_0 is simply estimated in this paper by averaging the observed image \mathbf{S} .

Finally, the prior $p(\mathbf{I})$ is written as:

$$p(\mathbf{I}) = p_1(\mathbf{I})p_2(\mathbf{I}). \quad (6)$$

In this section, different realistic priors on both illumination and reflectance are used to establish the probabilistic model. In the next section, we will show that formulating in the linear domain is more appropriate than in the logarithmic domain.

III. ANALYSIS OF THE LOGARITHMIC TRANSFORMATION

Converting $\mathbf{S} = \mathbf{R} \cdot \mathbf{I}$ into the logarithmic domain, we have: $\mathbf{s} = \mathbf{i} + \mathbf{r}$, where $\mathbf{s} = \log(\mathbf{S})$, $\mathbf{i} = \log(\mathbf{I})$ and $\mathbf{r} = \log(\mathbf{R})$. From this equation, one variable can be estimated by simple subtraction once the other variable is known. Kimmel was the first one to introduce the variational interpretation for Retinex based on the logarithmic transformation [29]. The author establishes the variational model only with illumination. Once the illumination \mathbf{i} is obtained, the reflectance \mathbf{r} can be estimated using $(\mathbf{s} - \mathbf{i})$. Other variational methods [30], [37] are proposed to use both illumination and reflectance in the objective function, which makes the model more appropriate for the estimation. Although experimental results presented in [30] and [37] show better performance than Kimmel's method [29], the direct estimated reflectance, i.e., some finer details of edges and textures, are usually smoothed out to end up with an inaccurate estimation.

Contradicting to conventional wisdom in light of the Weber's law [38], the new formulation employs the linear domain representation instead of log-transformed domain representation that are used in all existing variational models for decomposing reflectance and illumination including [29], [30], and [37]. We argue that while the log-transform is a proper transform to conform with human perception as described in the Weber's law, it is **not** a good transform to evaluate the variational cost that represents the prior information, i.e., to form the regularization terms in the variational model. Note that such variational cost terms are generally represented by a norm that evaluate a trade-off cost among different image areas. More specifically, given a target stimulus signal x , its gradient variation in the linear domain is ∇x , and its gradient variation in the log-transformed domain is then $\nabla(\log(x)) = \frac{1}{x}\nabla x$. That is to say, when x is very small, the gradient variation in the log-transformed domain $\nabla(\log(x))$ is highly weighted, i.e., by $\frac{1}{x}$, and therefore highly sensitive to the absolute gradient variation ∇x in the linear domain. This is



Fig. 1. Example of logarithmic transformation. (a) The observed image; (b) the logarithmic transformation of (a).

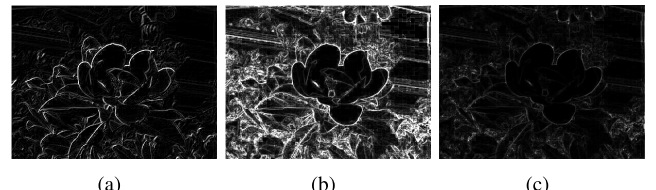


Fig. 2. (a) Gradients of Fig. 1(a), i.e., ∇x ; (b) gradients of Fig. 1(b) without normalization, i.e., $\nabla(\log(x)) = \frac{1}{x}\nabla x$; (c) normalized gradients of Fig. 1(b).

a good description for human perception represented by the Weber's law, since when the magnitude of the stimuli is low, we are very sensitive to the difference. However, when the highly weighted variation $\nabla(\log(x)) = \frac{1}{x}\nabla x$ is used in a norm, it is inevitably becoming dominant over the variation term in the high magnitude stimuli signal areas. It is apparently **undesirable** when we are trying to estimate/recover the fine structure in the high magnitude stimuli areas. On the other hand, the variation cost measure in the linear domain does not have such problems. Such phenomena are illustrated in the image example shown in Figs. 1 and 2. As can be seen in Fig. 2(b), many undesired structure are amplified in the low magnitude stimuli areas without normalization in the log-transformed domain, which indicate highly weight by $\frac{1}{x}$. Moreover, if we normalize Fig. 2(b) to generate Fig. 2(c), we can easily see that the intensity of fine edges and details in high illumination areas is buried in irrelevant details in low illumination areas and becomes too small to be used for estimating/recoverring fine structures due to intensities scaling. Obviously, such phenomena does not happen in the linear domain shown in Fig. 2(a).

To preserve edges and details, the existing methods described above must use the estimated illumination to obtain the reflectance using $\mathbf{R} = \mathbf{S}/\mathbf{I}$, where “/” denotes element-wise division. However, any error in estimated illumination at one pixel, denoted as Δi , will affect the estimated reflectance at the same location. The error in R caused by Δi is shown in equation (7).

$$\begin{aligned} |\Delta R| &= \left| \frac{S}{\tilde{I} + \Delta I} - \frac{S}{\tilde{I}} \right| = \left| \frac{e^s}{e^{\tilde{i} + \Delta i}} - \frac{e^s}{e^{\tilde{i}}} \right| \\ &= \left| \frac{e^s}{e^{\tilde{i}}} \left(\frac{1}{e^{\Delta i}} - 1 \right) \right| = \left| \tilde{R}(e^{-\Delta i} - 1) \right|, \end{aligned} \quad (7)$$

where \tilde{I} and \tilde{R} denote the actual illumination and reflectance at one pixel, ΔI is the error in estimated illumination in the linear domain caused by Δi and \tilde{i} denotes the actual illumination in the logarithmic domain. Equation (7) indicates

that Δi will exponentially affect $|\Delta R|$. Once the estimated illumination is inaccurate, so is the reflectance. Moreover, since both reflectance and enhanced result rely on the estimated illumination, conventional methods for decomposing reflectance and illumination cannot handle noise effectively. Relevant experiments are shown in Fig. 14.

Intuitively, a method which can estimate illumination and reflectance simultaneously and accurately should be considered. Based on the above analysis, it is clear that solving the problem directly in the linear domain is more appropriate than in the logarithmic domain. In the next section, an efficient optimization strategy is adopted to estimate illumination and reflectance simultaneously.

IV. OPTIMIZATION ALGORITHM

To efficiently estimate illumination and reflectance simultaneously, the MAP problem is transformed into an energy minimization problem, i.e., $E(\mathbf{I}, \mathbf{R}) = -\log(p(\mathbf{I}, \mathbf{R} | \mathbf{S}))$. The objective function is established by taking all likelihood and priors into consideration:

$$E(\mathbf{I}, \mathbf{R}) = \|\mathbf{R} \cdot \mathbf{I} - \mathbf{S}\|_2^2 + \alpha \|\nabla \mathbf{I}\|_2^2 + \beta \|\nabla \mathbf{R}\|_1 + \gamma \|\mathbf{I} - \mathbf{I}_0\|_2^2 \quad s.t. \quad \mathbf{S} \leq \mathbf{I}, \quad (8)$$

where α , β , and γ are three positive parameters and $\|\cdot\|_p$ denotes the p -norm operator. Additionally, since the value of \mathbf{R} is between 0 and 1, the function is subject to the constraint: $\mathbf{S} \leq \mathbf{I}$. To minimize $E(\mathbf{I}, \mathbf{R})$, for the first term ($\|\mathbf{R} \cdot \mathbf{I} - \mathbf{S}\|_2^2$), which corresponds to L2 data fidelity, is to minimize the distance between estimated ($\mathbf{R} \cdot \mathbf{I}$) and observed image \mathbf{S} . The second term ($\|\nabla \mathbf{I}\|_2^2$) enforces spatial smoothness on the illumination \mathbf{I} . The third term ($\|\nabla \mathbf{R}\|_1$), which corresponds to TV reflectance sparsity, enforces piece-wise continuous on the reflectance \mathbf{R} . The last term ($\|\mathbf{I} - \mathbf{I}_0\|_2^2$), which is based on the L2 white patch assumption, is used to avoid a scaling problem. All the terms in (8) correspond to the posterior distribution in section II.

Since there are two unknowns in (8), traditional gradient descent methods are unusable. In this paper, an alternating direction method of multipliers (ADMM) [39] is adopted to find a local optimal solution to the non-convex objective function in (8). Since an L1-norm is hard to solve, an auxiliary variable \mathbf{d} and an error \mathbf{b} are introduced and function (8) is rewritten as:

$$E(\mathbf{I}, \mathbf{R}, \mathbf{d}, \mathbf{b}) = \|\mathbf{R} \cdot \mathbf{I} - \mathbf{S}\|_2^2 + \alpha \|\nabla \mathbf{I}\|_2^2 + \beta \{\|\mathbf{d}\|_1 + \lambda \|\nabla \mathbf{R} - \mathbf{d} + \mathbf{b}\|_2^2\} + \gamma \|\mathbf{I} - \mathbf{I}_0\|_2^2 \quad s.t. \quad \mathbf{S} \leq \mathbf{I}. \quad (9)$$

This objective function will have local minima, according to ADMM theory [39]. Three separate sub-problems are iteratively cycled through. In particular, for the j th iteration:

$$(P1) \quad \mathbf{d}^j = \arg \min_{\mathbf{d}} \|\mathbf{d}\|_1 + \lambda \left\| \nabla \mathbf{R}^{j-1} - \mathbf{d} + \mathbf{b}^{j-1} \right\|_2^2,$$

$$(P2) \quad \mathbf{R}^j = \arg \min_{\mathbf{R}} \left\| \mathbf{R} - \frac{\mathbf{S}}{\mathbf{I}^{j-1}} \right\|_2^2 + \beta \lambda \left\| \nabla \mathbf{R} - \mathbf{d}^j + \mathbf{b}^{j-1} \right\|_2^2, \\ \mathbf{b}^j = \mathbf{b}^{j-1} + \nabla \mathbf{R}^j - \mathbf{d}^j,$$

$$(P3) \quad \mathbf{I}^j = \arg \min_{\mathbf{I}} \left\| \mathbf{I} - \frac{\mathbf{S}}{\mathbf{R}^j} \right\|_2^2 + \alpha \|\nabla \mathbf{I}\|_2^2 + \gamma \|\mathbf{I} - \mathbf{I}_0\|_2^2.$$

Note that we transform $\|\mathbf{R} \cdot \mathbf{I}^{j-1} - \mathbf{S}\|_2^2$ into $\left\| \mathbf{R} - \frac{\mathbf{S}}{\mathbf{I}^{j-1}} \right\|_2^2$ in (P2) for the convenience of calculation. The similar operation is also applied in (P3). The three sub-problems have closed form global optimal solutions. The update for \mathbf{b}^j follows from ADMM. The algorithm is detailed as follows:

1) *Algorithm for P1:* Initializing $\mathbf{b}^0 = 0$ and $\mathbf{R}^0 = 0$, a shrinkage operation is adopted to update \mathbf{d}^j at the j th iteration:

$$\begin{aligned} \mathbf{d}_h^j &= \text{shrink}(\nabla_h \mathbf{R}^{j-1} + \mathbf{b}_h^{j-1}, \frac{1}{2\lambda}), \\ \mathbf{d}_v^j &= \text{shrink}(\nabla_v \mathbf{R}^{j-1} + \mathbf{b}_v^{j-1}, \frac{1}{2\lambda}), \end{aligned} \quad (10)$$

where $\text{shrink}(x, \lambda) = \frac{x}{|x|} * \max(|x| - \lambda, 0)$ with $\frac{x}{|x|}$ equal to 0 when $|x| = 0$. h and v are the horizontal and vertical directions, respectively.

2) *Algorithm for P2:* \mathbf{I}^0 is initialized using Gaussian low-pass filtering of the observed image, which is similar to center/surround Retinex methods [2], [3], [28]. Since P2 is a least squares problem, \mathbf{R}^j has a closed form solution. The Fast Fourier Transformation (FFT) is adopted to speed up the process, which is similar to other methods [30], [39]. By setting the first-order derivative to zero, \mathbf{R}^j is updated by the following expression in the frequency domain:

$$\mathbf{R}^j = F^{-1} \left(\frac{F(\mathbf{S}/(\mathbf{I}^{j-1} + \Delta)) + \beta \lambda \Phi}{F(\mathbf{1}) + \beta \lambda (F^*(\nabla_h) \cdot F(\nabla_h) + F^*(\nabla_v) \cdot F(\nabla_v))} \right), \quad (11)$$

where $\Phi = F^*(\nabla_h) \cdot F(\mathbf{d}_h^j - \mathbf{b}_h^{j-1}) + F^*(\nabla_v) \cdot F(\mathbf{d}_v^j - \mathbf{b}_v^{j-1})$, Δ is a small positive value used to avoid the denominator being 0, F is the FFT operator, F^* is the conjugate transpose and F^{-1} is the inverse FFT operator. The derivative operator is diagonalized after FFT so that matrix inversion can be avoided. All calculations are performed element-wise.

Updating \mathbf{b}^j by the following expression at the j th iteration:

$$\begin{aligned} \mathbf{b}_h^j &= \mathbf{b}_h^{j-1} + \nabla_h \mathbf{R}^j - \mathbf{d}_h^j, \\ \mathbf{b}_v^j &= \mathbf{b}_v^{j-1} + \nabla_v \mathbf{R}^j - \mathbf{d}_v^j. \end{aligned} \quad (12)$$

This operation is the similar to “adding back the noise” used in TV denoising [40]. \mathbf{d} , \mathbf{R} and \mathbf{b} are updated until $\epsilon_R = (\|\mathbf{R}^j - \mathbf{R}^{j-1}\| / \|\mathbf{R}^{j-1}\|) \leq \epsilon_1$.

3) *Algorithm for P3:* Updating \mathbf{I}^j is similar to \mathbf{R}^j since P3 is also a least squares problem:

$$\mathbf{I}^j = F^{-1} \left(\frac{F(\gamma \mathbf{I}_0 + \mathbf{S}/(\mathbf{R}^j + \Delta))}{F(\mathbf{1}) + \gamma + \alpha (F^*(\nabla_h) \cdot F(\nabla_h) + F^*(\nabla_v) \cdot F(\nabla_v))} \right). \quad (13)$$

According to the prior: $\mathbf{S} \leq \mathbf{I}$, a simple correction is made after \mathbf{I} is updated: $\mathbf{I}^j = \max(\mathbf{I}^j, \mathbf{S})$. \mathbf{I} is updated until $\epsilon_I = (\|\mathbf{I}^j - \mathbf{I}^{j-1}\| / \|\mathbf{I}^{j-1}\|) \leq \epsilon_2$.

Since large-matrix inversion is avoided by FFT and the shrinkage operation is fast due to requiring only a few operations, \mathbf{I} and \mathbf{R} can be solved simultaneously and efficiently.

In the end, the proposed algorithm is summarized in **Algorithm 1**. What is more, the existence of a solution to

Algorithm 1 Outline of Algorithm

Input: observed image \mathbf{S} , parameters α , β , γ and λ ,
stopping parameters ε_1 and ε_2 .

Initialization: $\mathbf{I}^0 \leftarrow$ Gaussian filtering of \mathbf{S} , $\mathbf{R}^0 = 0$, $\mathbf{b}^0 = 0$,
 $I_0 \leftarrow$ average of \mathbf{S} , set $j = 1$.

At the j -th iteration:

- update \mathbf{d}^j using (10).
- update \mathbf{R}^j using (11).
- update \mathbf{b}^j using (12).
- update \mathbf{I}^j using (13).
- correct \mathbf{I}^j using $\max(\mathbf{I}^j, \mathbf{S})$.

Stopping criteria: if $\varepsilon_R \leq \varepsilon_1$ and $\varepsilon_I \leq \varepsilon_2$, stop iteration,
otherwise $j = j + 1$ and continue the iteration.

Output: illumination \mathbf{I} , reflectance \mathbf{R} .

the minimization problem (8) is proved in **Appendix A**. In the next section, experimental results are presented to demonstrate the efficiency and effectiveness of the proposed method.

V. EXPERIMENTAL RESULTS

In this section, experimental results are presented to illustrate the efficiency and effectiveness of the proposed method. The simulation is Matlab R2012a on a PC with a 2.60GHz Intel Pentium Dual Core Processor. The Matlab code can be found on our website: <http://smartdsp.xmu.edu.cn/Appendix.html>.

Since the reflectance is sometimes over-enhanced [29], [30], [37], a Gamma correction operation is adopted for post-processing, similar to previous studies [29], [30], [37]. The Gamma correction of the illumination \mathbf{I} with an adjustment parameter γ' is defined as follows:

$$\mathbf{I}' = W \left(\frac{\mathbf{I}}{W} \right)^{\frac{1}{\gamma'}}, \quad (14)$$

where W is 255 and the empirical parameter γ' is set as 2.2. The final enhanced image is:

$$\mathbf{S}_{\text{enhanced}} = \mathbf{R} \cdot \mathbf{I}'. \quad (15)$$

In our experiments, the empirical parameters α , β , γ and λ are set at 1000, 0.01, 0.1 and 10, respectively. The analysis of parameter selection is shown in the experiments presented later. For the stopping parameters, ε_1 and ε_2 are set to be 0.1. Two approaches [30] can be used with the proposed method for color images. The first one is to process each RGB (red, green, and blue) channel separately. The second is to transform color images into the HSV (hue, saturation and value) space and only process the V layer, and then transform it back to the RGB-color space. When an image contains both severe color distortion and dark appearance, the visual effect of results that processed in the RGB-color space will be better than that in the HSV-color space. For simplification, the HSV algorithm is adopted to process images unless specifically indicated in the following experiments. Results of the proposed method are compared with other relevant algorithms for different images.

Fig. 3 shows the experimental results obtained using the proposed method in both RGB-color space and HSV-color space.

It can be seen that the illuminations in Figs. 3(b) and 3(e) exhibit spatial smoothing. Fig. 3(b) includes color information since the algorithm is applied to each RGB channel separately. Moreover, processing in the RGB-color space can make color correction as shown in the following experiments, i.e., Figs. 7 and 8. The reflectance in Figs. 3(c) and 3(f) effectively preserve the edges while Fig. 3(c) contains color information. Figs. 3(d) and 3(g) show the final enhanced images with Gamma correction. This operation can lighten the observed image and avoid over-enhancement and provides a good visual quality to the images.

Now we compare the proposed method with other relevant state-of-the-art methods. Four Retinex methods, including the MSRCR method [2], Kimmel's method [29], Ng's method [30] and Bayesian method [37], and two non-Retinex methods, including the classical histogram equalization (HE) [41] and the automatic color enhancement (ACE) [42] are used for comparison. The scale parameters are 15, 80 and 250 in the MSRCR. In Kimmel's method and Ng's method, the parameters are set the same as in [29] and [30], i.e., $\alpha = 1$, $\beta = 0.1$, $\mu = 10^{-5}$, $\lambda = 1$. In the Bayesian method [37], the maximum number of iterations is set at 50 and the stopping criterion parameter is set as 10^{-4} . The slope parameter is set to 5 in the ACE method [42].

Due to space limitations, three images selected for illustration, since they include different conditions such as long shot, close shot, non-uniform illumination and night-time. It can be seen that the HE method, shown in Figs. 4(b)-6(b) produces over-enhancement and color distortion, i.e., the long shot in Fig. 4(b), the sky in Fig. 5(b) and the lighting region in Fig. 6(b). The ACE method, in Figs. 4(c)-6(c), also has an unsatisfactory effect on color and is very sensitive to the spatial weighting. The MSRCR has some over-enhancement effects as can be observed by effects such as the whitening of the blue sky in Fig. 4(d) and the lighting region on the desk in Fig. 6(d). The subjective visual effect of the proposed method is similar to the other three variational methods [29], [30], [37]. However, the proposed method produces a better contrast than these three methods, as shown in the following objective assessment. The enhancements produced by the proposed method have better color range, lightened dark regions, naturalness preservation, and effectively enhanced details.

Three objective metrics are further presented to evaluate the enhanced results in Figs. 4-6. The averages of evaluation scores are also calculated for overall comparison. The first metric is the contrast gain based on the contrast difference between the observed image and the enhanced result. A higher value means a better contrast. The formula for the gain is:

$$G = \frac{C_{\text{enhanced}}}{C_{\text{observed}}}, \quad (16)$$

where C is the average value of 3×3 local contrast obtained by Michelson contrast [43]. Table 1 shows quantitative measurement results of the contrast gain. As shown in Table 1, HE and MSRCR have a higher average contrast gain than the proposed method, since both methods stretch the dynamic



Fig. 3. Proposed method in both RGB-color space and HSV-color space. (a) The observed image; (b) the illumination image in RGB-color space; (c) the reflectance image in RGB-color space; (d) the enhanced image using Gamma correction with (b) and (c); (e) the illumination image in HSV-color space; (f) the reflectance image in HSV-color space; (g) the enhanced image using Gamma correction with (e) and (f).

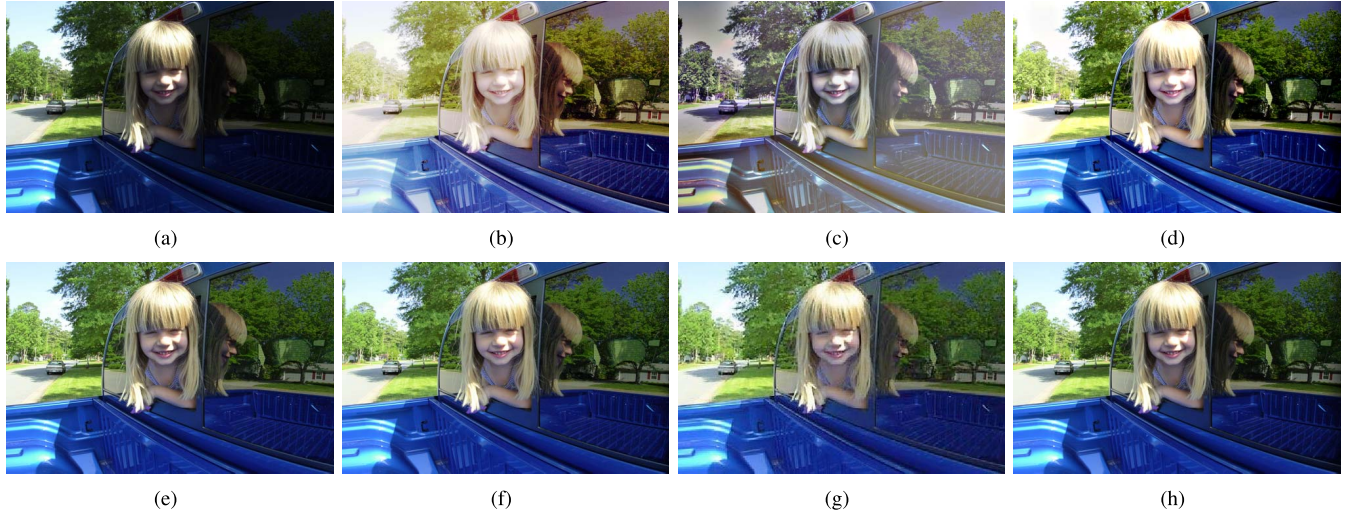


Fig. 4. **Girl image.** (a) the observed image; (b) The result by HE [41]; (c) the result by ACE [42]; (d) the result by MSRCR [2]; (e) the result by Kimmel's method [29]; (f) the result by Ng's method [30]; (g) the result by Bayesian method [37]; (h) the result by the proposed method.

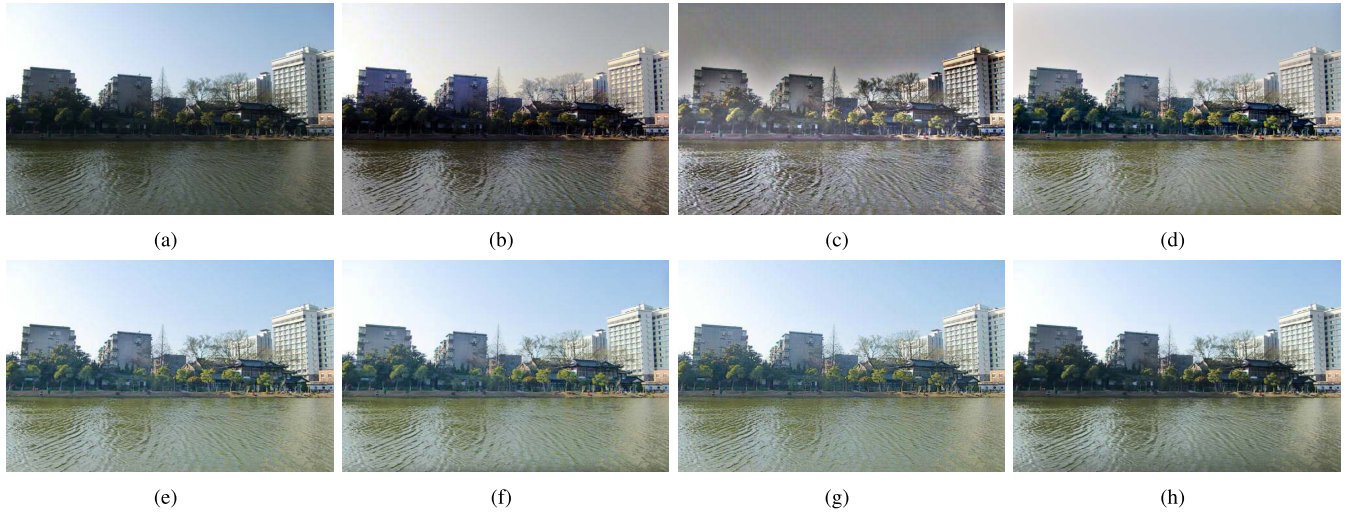


Fig. 5. **Landscape image.** (a) The observed image; (b) the result by HE [41]; (c) the result by ACE [42]; (d) the result by MSRCR [2]; (e) the result by Kimmel's method [29]; (f) the result by Ng's method [30]; (g) the result by Bayesian method [37]; (h) the result by the proposed method.

range to increase the contrast. However, the subjective visual effect of the proposed method is obviously better than MSRCR and HE.

The second metric is the lightness-order-error (LOE) measure [5], shown in Table 2 to evaluate naturalness preservation. This evaluation is based on the following constraint: the

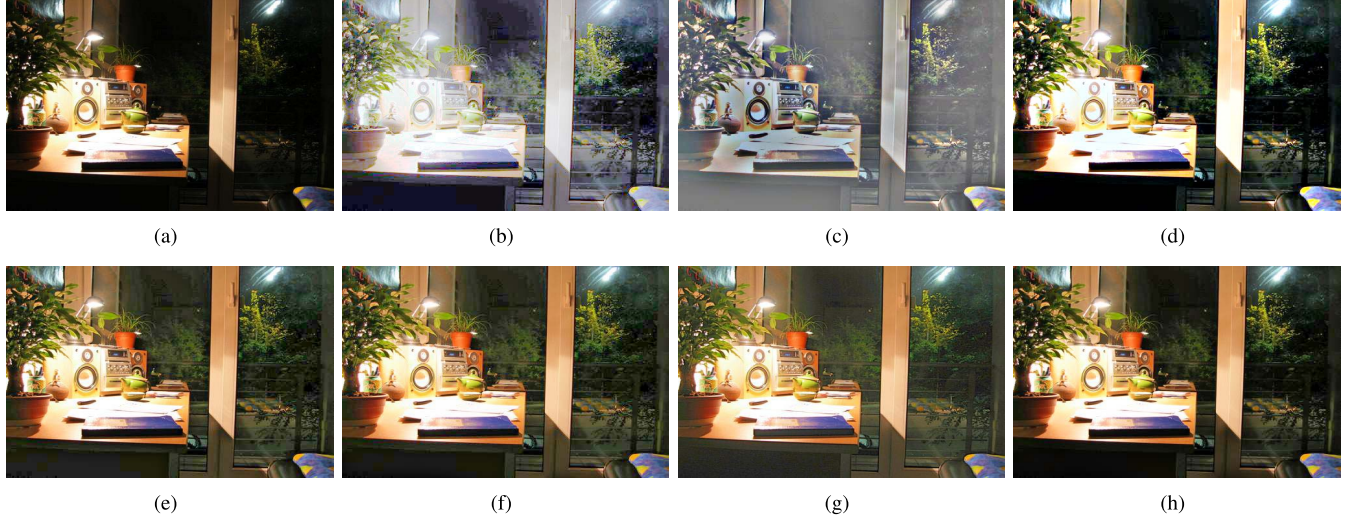


Fig. 6. **Desk image.** (a) The observed image; (b) the result by HE [41]; (c) the result by ACE [42]; (d) the result by MSRCR [2]; (e) the result by Kimmel's method [29]; (f) the result by Ng's method [30]; (g) the result by Bayesian method [37]; (h) the result by the proposed method.

TABLE I
QUANTITATIVE MEASUREMENT RESULTS OF CONTRAST GAIN

| | HE [41] | ACE [42] | MSRCR [2] | Kimmel's method [29] | Ng's method [30] | Bayesian method [37] | The proposed method |
|----------------|---------|----------|-----------|----------------------|------------------|----------------------|---------------------|
| Girl | 0.85 | 0.61 | 1.30 | 0.89 | 0.88 | 0.76 | 0.93 |
| Landscape | 1.41 | 1.18 | 1.12 | 0.86 | 0.82 | 0.82 | 0.92 |
| Desk | 0.72 | 0.49 | 1.38 | 0.91 | 0.85 | 0.62 | 0.95 |
| Average | 0.99 | 0.76 | 1.27 | 0.89 | 0.85 | 0.73 | 0.93 |

TABLE II
QUANTITATIVE MEASUREMENT RESULTS OF LOE

| | HE [41] | ACE [42] | MSRCR [2] | Kimmel's method [29] | Ng's method [30] | Bayesian method [37] | The proposed method |
|----------------|---------|----------|-----------|----------------------|------------------|----------------------|---------------------|
| Girl | 5.4 | 39.7 | 7.7 | 7.0 | 4.2 | 12.5 | 5.6 |
| Landscape | 2.6 | 58.1 | 13.4 | 7.7 | 6.2 | 10.8 | 6.7 |
| Desk | 7.5 | 48.3 | 12.4 | 13.9 | 9.2 | 13.2 | 8.8 |
| Average | 5.2 | 48.7 | 11.2 | 9.5 | 6.5 | 12.2 | 7.0 |

TABLE III
QUANTITATIVE MEASUREMENT RESULTS OF NIQE

| | HE [41] | ACE [42] | MSRCR [2] | Kimmel's method [29] | Ng's method [30] | Bayesian method [37] | The proposed method |
|----------------|---------|----------|-----------|----------------------|------------------|----------------------|---------------------|
| Girl | 1.69 | 2.04 | 1.86 | 2.63 | 2.03 | 2.76 | 2.03 |
| Landscape | 3.27 | 3.18 | 3.29 | 3.53 | 3.36 | 3.75 | 3.27 |
| Desk | 2.90 | 2.32 | 2.51 | 2.52 | 2.48 | 2.01 | 2.25 |
| Average | 2.62 | 2.51 | 2.55 | 2.90 | 2.62 | 2.84 | 2.52 |

relative lightness order is related to the naturalness and should not be changed rapidly in the enhanced image [5]. A smaller LOE value means a smaller change in the relative lightness order, representing better naturalness preservation. As shown in Table 2, the proposed method outperforms ACE, MSRCR, Kimmel's method and Bayesian method in preserving the naturalness. Although HE and Ng's method have a slight lower LOE value, the proposed method shows a better local contrast than Ng's method, and a better overall visual effect than HE.

The third metric is the natural image quality evaluator (NIQE) blind image quality assessment [44], which is

based on statistical regularities from natural and undistorted images. A lower NIQE value represents a higher image quality. As shown in Table 3, the proposed method has a lower average than other algorithms except ACE. However, ACE has the highest average of LOE measure in Table 2 which indicates the worst performance on naturalness preservation. In contrast, the proposed method has a stable objective performance over the three metrics.

In next two experiments, color correction and reflectance estimation are tested to demonstrate the advantages of formulating in the linear domain instead of the logarithmic domain.



Fig. 7. Comparison of color correction. (a) The observed image; (b) the ground truth; (c) the result by Kimmel's method [29]; (d) the enhanced image by Ng's method [30]; (e) the result by the proposed method.



Fig. 8. Comparison of color correction. (a) The observed image; (b) the ground truth; (c) the result by Kimmel's method [29]; (d) the enhanced image by Ng's method [30]; (e) the result by the proposed method.

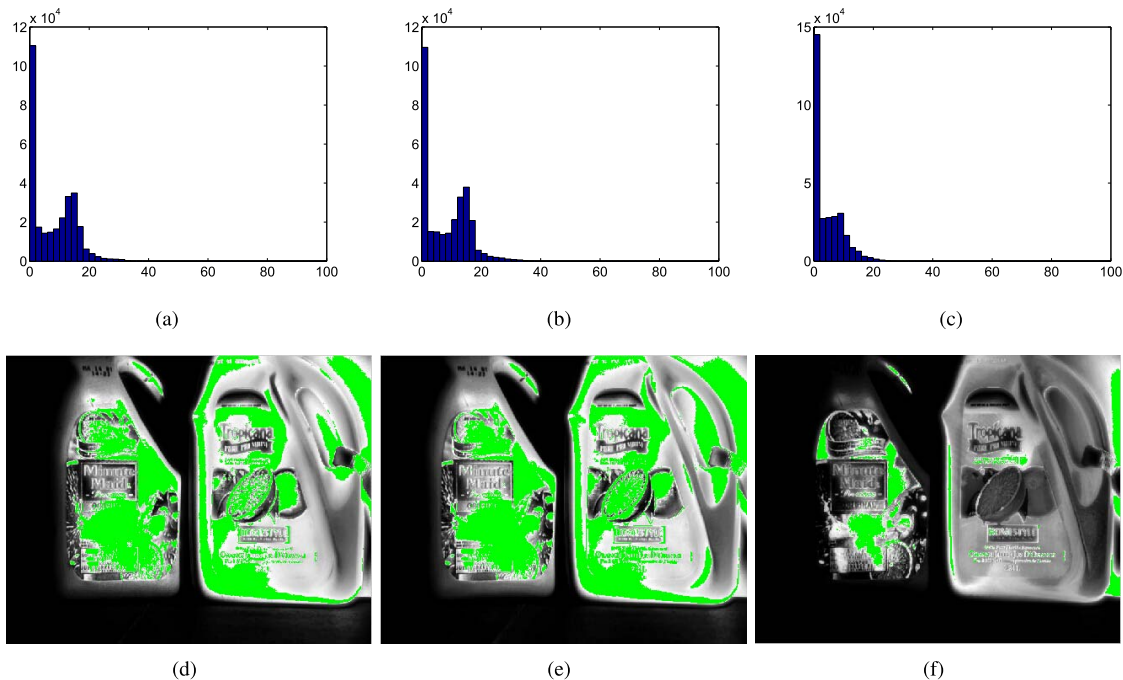


Fig. 9. (a)-(c) The histogram distribution of S-CIELAB errors of Fig. 7(b) (ground truth) with Fig. 7(c) (Kimmel's method [29]), Fig. 7(d) (Ng's method [30]), Fig. 7(e) (the proposed method), respectively; (d)-(e) the spatial location of the errors, that are 15 units or higher marked by green, between Fig. 7(b) and Fig. 7(c), Fig. 7(d), Fig. 7(e), respectively.

In Figs. 7 and 8, we focus on the color correction performance to demonstrate the accuracy of the estimated illumination. Since the illumination is computed in the RGB-color space and removed, the reflectance retains the original color information of the object, meaning that the proposed algorithm has the effect of color correction. The original images are processed in the RGB-color space and the results are compared with two other Retinex algorithms [29], [30]. Original images and actual illuminants are downloaded from

http://colorconstancy.com/?page_id=21. Compared with the other two algorithms, Figs. 7(e) and 8(e) show an obvious color correction effect using the proposed method. For instance, see the color of orange bottle in Fig. 7 and the color of wall and books in Fig. 8. The S-CIELAB color metric [45] based on spatial processing to measure color errors, is then adopted to verify the accuracy of color correction. The S-CIELAB errors between the ground truth and different algorithms are shown in Figs. 9 and 10. As can be seen, the

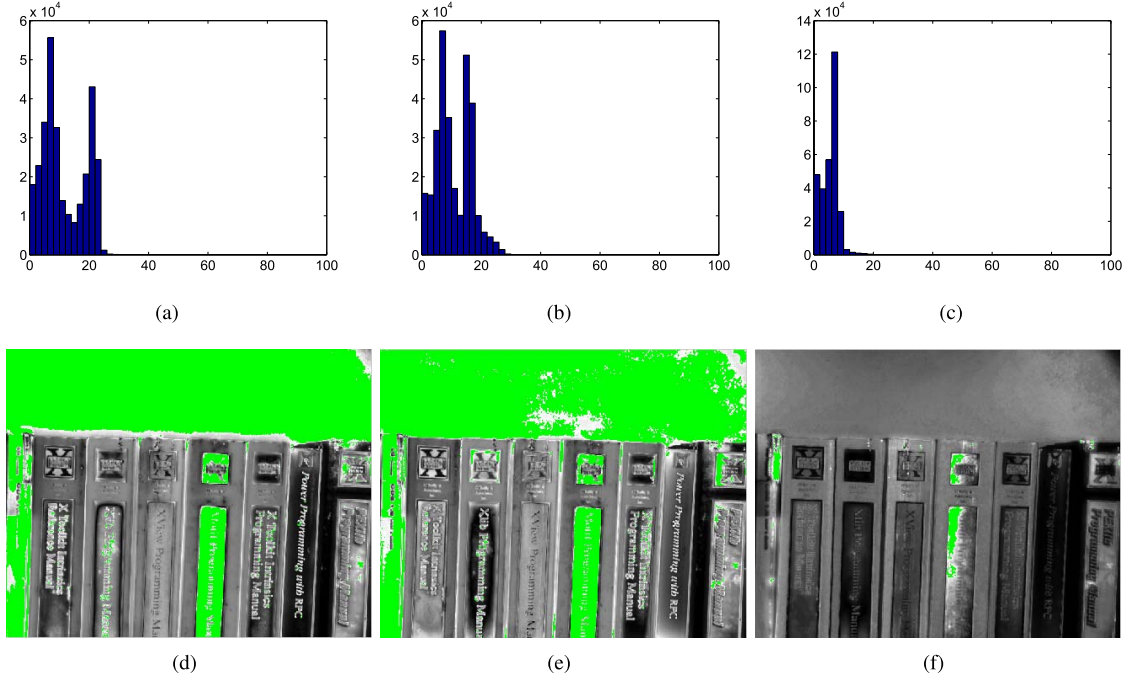


Fig. 10. (a)-(c) The histogram distribution of S-CIELAB errors of Fig. 8(b) (ground truth) with Fig. 8(c) (Kimmel's method [29]), Fig. 8(d) (Ng's method [30]) and Fig. 8(e) (the proposed method), respectively; (d)-(e) the spatial location of the errors, that are 15 units or higher marked by green, between Fig. 8(b) and Fig. 8(c), Fig. 8(d), Fig. 8(e), respectively.

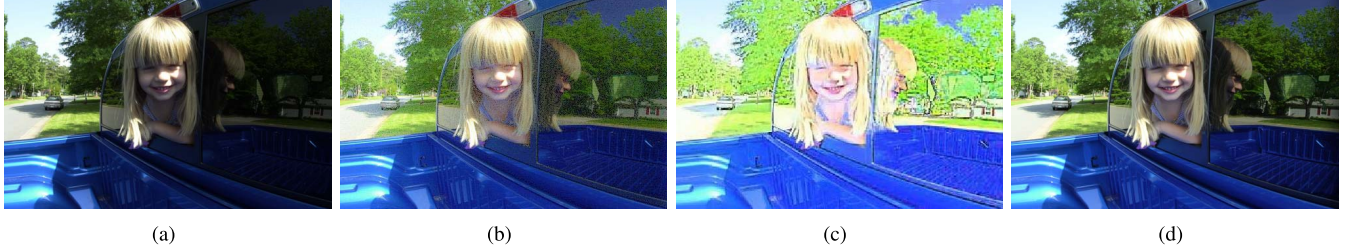


Fig. 11. Comparison of reflectance estimation. (a) The observed image; (b) Gamma correction with the reflectance directly derived from Ng's method [30]; (c) Gamma correction with the reflectance directly derived from Bayesian method [37]; (d) Gamma correction with the reflectance directly derived from the proposed method.



Fig. 12. Comparison of reflectance estimation. (a) The observed image; (b) Gamma correction with the reflectance directly derived from Ng's method [30]; (c) Gamma correction with the reflectance directly derived from Bayesian method [37]; (d) Gamma correction with the reflectance directly derived from the proposed method.

numbers of pixels per error unit are given by the histogram distribution of S-CIELAB. From the histogram distribution, we can conclude that the difference between the ground truth and the processed image using the new method is smaller than all other algorithms. This can be seen by the spatial locations of the errors, marked in green in Figs. 9 and 10.

Subsequently, the quality of reflectance estimation is validated. The results are compared with other two variational Retinex methods [30], [37], both estimating reflectance. Figs. 11 and 12 show the results of Gamma correction with the reflectance directly derived from different algorithms. It can be seen that the reflectance directly derived from

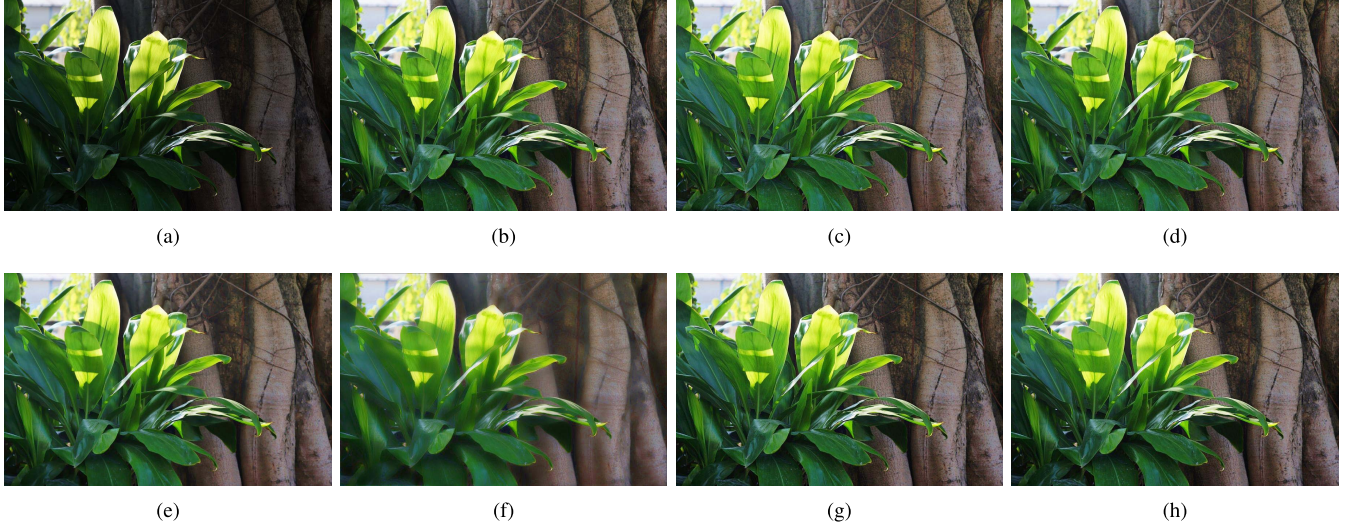


Fig. 13. The effects of regularization parameters. (a) The observed image. (b) $\alpha = 1000$, $\beta = 0.01$, $\gamma = 0.1$. (c) $\alpha = 10$, $\beta = 0.01$, $\gamma = 0.1$. (d) $\alpha = 100$, $\beta = 0.01$, $\gamma = 0.1$. (e) $\alpha = 1000$, $\beta = 0.1$, $\gamma = 0.1$. (f) $\alpha = 1000$, $\beta = 1$, $\gamma = 0.1$. (g) $\alpha = 1000$, $\beta = 0.01$, $\gamma = 1$. (h) $\alpha = 1000$, $\beta = 0.01$, $\gamma = 10$.

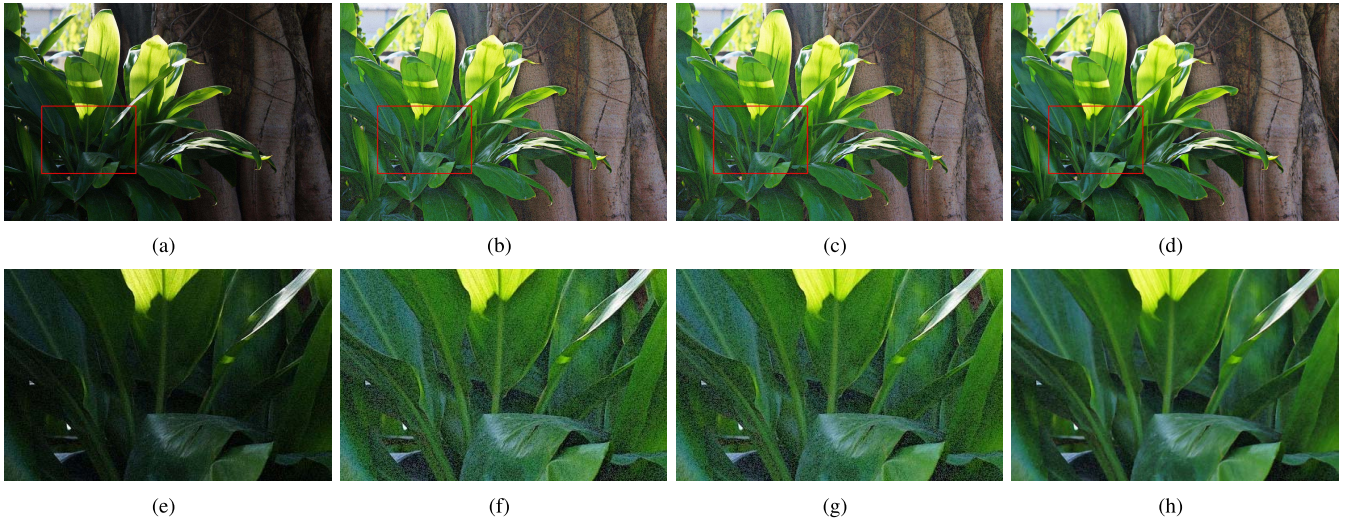


Fig. 14. Comparison of noise suppression. (a) The noisy image of Fig. 13(a); (b) Gamma correction of Kimmel's method [29]; (c) Gamma correction of Ng's method [30]; (d) Gamma correction of the proposed method; (e)-(h): enlargements of (a)-(d) in the red rectangle.

algorithm [30], [37] are over-enhanced and over-smoothed, while the proposed new method performs better on edges and naturalness preservation, such as the girl's eyes in Fig. 11 and the leaves on the trees in Fig. 12. This experiment demonstrates that estimating reflectance in the linear domain is more appropriate than the logarithmic domain, since the logarithmic transformation smoothes edges and amplifies undesired structure in low illumination areas, as discussed in section III. On the contrary, the proposed method can estimate the reflectance more accurately than the other two algorithms. This is because formulating in the linear domain can better represent prior information for better estimation of reflectance.

Next, the effects of regularization parameters α , β and γ in model (8) are tested. The empirical parameters are set as 1000, 0.01 and 0.1 as shown in Fig. 13(b). First, β and γ are fixed at 0.01 and 0.1, respectively, and α varies between 10 and 100. In Fig. 13(c)-(d), the illuminations of the enhanced results are

weakened slightly as α increases. This is because α controls the smoothness of the illumination. Then α and γ are fixed at 1000 and 0.1, respectively, and β is varied between 0.1 and 1. Fig. 13(e)-(f) shows edges are fuzzed since L1 term decreases as β increases. However, the effect of β can be used to handle noise, shown in the next experiment. Finally, α and β are fixed at 1000 and 0.01, respectively, and γ is varied between 1 and 10. Fig. 13(g)-(h) show the enhanced results that are almost unchanged. In most cases, the empirical setting of regularization parameters generates satisfactory results.

In this experiment, the effectiveness of noise suppression is tested by comparing with Kimmel's method [29] and Ng's method [30]. The parameter β of the proposed method is set as 0.05 for a better visualization. The image in Fig. 13(a) is contaminated with slight additive white Gaussian noise \mathbf{n} with $\sigma = 5$. Due to the reflectance estimated by methods [29], [30] is inaccurate, the Gamma correction only relies on the

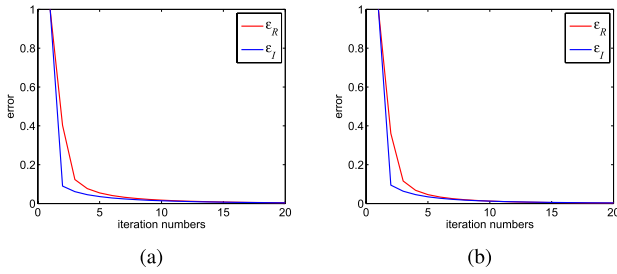


Fig. 15. The relation between the error ε_R , ε_I and the number of iterations.
 (a) image with size 300×197 ; (b) image with size 1200×787 .

estimated illumination, i.e.,

$$\mathbf{S}_{enhanced} = \frac{\mathbf{S}}{\mathbf{I}} \cdot \mathbf{I}' = (\mathbf{R} \cdot \mathbf{I} + \mathbf{n}) \cdot \frac{\mathbf{I}'}{\mathbf{I}}. \quad (17)$$

However, since $\mathbf{I} \leq \mathbf{I}'$ according to equation (14), noise will be amplified after Gamma correction, especially in dark regions. As can be seen in Figs. 14(f) and 14(g), both Kimmel's method [29] and Ng's method [30] amplify the noise after Gamma correction. While the proposed method can suppress noise without losing enhancing effect, as shown in Fig. 14(h). Since the proposed method solving the problem in the linear domain and estimates reflectance and illumination simultaneously, the L1 regularization term in equation (8) can effectively handle noise.

The convergence of the proposed optimization algorithm is analyzed in this set of experiments. Two different images with different sizes 300×197 and 1200×787 are tested. Fig. 15 shows the relationship between the error ε_R , ε_I and the number of iterations. As can be seen, the convergence rate is fast and independent of the image size. Both errors ε_R and ε_I in the images are less than 0.01 after nearly 12 iterations. This phenomenon is due to the optimization algorithm which effectively splits the energy minimization problem into two convex sub-problems which optimizes R and I . Fig. 15 demonstrates the convergence of the proposed algorithm.

The last experiment tests the computational time of the proposed method. Since all calculations of the proposed algorithm are element-wise and the FFT is adopted to avoid large-matrix inversion, the computational time is satisfactory. It takes about 1.8 seconds with size of 500×328 . Note that some methods, such as Bayesian method [37], have higher computational complexity due to the need to solve very large linear equations. The computational time of the proposed method can be further improved by C programming and advanced computing devices, such as a Graphics Processing Unit (GPU).

VI. CONCLUSION

In this paper, a new probabilistic method for image enhancement that estimates illumination and reflectance simultaneously is proposed in the linear domain. We show that formulating in the linear domain is more appropriate than in the logarithmic domain as described in section III. Firstly, based on the intrinsic properties of illumination and reflectance, an MAP based probabilistic model for estimating

illumination and reflectance is formulated in the linear domain instead of the commonly used logarithmic domain. To separate the illumination and the reflectance efficiently, the MAP problem is transformed into an energy minimization problem to fully use various image priors. An iterative optimization algorithm is introduced to solve the energy minimization problem and estimate the illumination and reflectance simultaneously and effectively. Experimental results present a comprehensive analysis of the proposed method using both subjective and objective assessments. Compared with several state-of-the-art algorithms, the proposed method shows similar or even better results with satisfactory computational cost.

APPENDIX

THE EXISTENCE FOR SOLUTION OF THE MINIMIZATION PROBLEM

Thanks to the literature [30], we are to prove the existence for the solution of the given minimization problem here.

First, a tiny value Δ is added with the observed image \mathbf{S} to prevent it from approaching 0 when \mathbf{S} is the denominator. So actually we have $\mathbf{S} = \mathbf{S} + \Delta$ and this will not affect the final result.

Supposed that S is defined on Ω . Then the feasible solution space can be

$$\Lambda = \left\{ (\mathbf{R}, \mathbf{I}) \mid (\mathbf{R}, \mathbf{I}) \in BV(\Omega) \times W^{1,2}(\Omega), \mathbf{S} \leq \mathbf{I} \right\}.$$

And, the energy minimization problem is

$$\begin{aligned} \min_{(\mathbf{R}, \mathbf{I}) \in \Lambda} E(\mathbf{R}, \mathbf{I}) = & \min_{(\mathbf{R}, \mathbf{I}) \in \Lambda} \|\mathbf{R} \cdot \mathbf{I} - \mathbf{S}\|_2^2 + \alpha \|\nabla \mathbf{I}\|_2^2 \\ & + \beta \|\nabla \mathbf{R}\|_1 + \gamma \|\mathbf{I} - I_0\|_2^2 \quad s.t. \quad \mathbf{S} \leq \mathbf{I}. \end{aligned} \quad (\text{A-1})$$

Theorem: Let $\mathbf{S} \in L^\infty(\Omega)$, the problem (A-1) has at least one solution.

Proof: If \mathbf{I} and \mathbf{R} are two constants, the energy $E(\mathbf{R}, \mathbf{I})$ will be finite. Assume $(\mathbf{R}_t, \mathbf{I}_t)$ is a minimizing sequence of problem (A-1), then there exists a constant $M > 0$ such that

$$E(\mathbf{R}_t, \mathbf{I}_t) < M,$$

So this inequality can be written as:

$$\|\mathbf{R}_t \cdot \mathbf{I}_t - \mathbf{S}\|_2^2 + \alpha \|\nabla \mathbf{I}_t\|_2^2 + \beta \|\nabla \mathbf{R}_t\|_1 + \gamma \|\mathbf{I}_t - I_0\|_2^2 \leq M.$$

The boundedness of either $\|\nabla \mathbf{I}_t\|_2^2$ or $\|\mathbf{I}_t - I_0\|_2^2$ guarantees that $\{\mathbf{I}_t\}$ is uniformly bounded in $W^{1,2}(\Omega)$. Note that $W^{1,2}(\Omega)$ is embedded in $L^2(\Omega)$, so up to a subsequence, $\{\mathbf{I}_t\}$ converges to a $\mathbf{I}_* \in W^{1,2}(\Omega)$, i.e.,

$$\mathbf{I}_t \xrightarrow[L^2(\Omega)]{} \mathbf{I}_* \text{ and } \mathbf{I}_t \rightharpoonup \mathbf{I}_* \in W^{1,2}(\Omega). \quad (\text{A-2})$$

Meanwhile, the sequence $\{\mathbf{R}_t\}$ satisfies

$$\beta \|\nabla \mathbf{R}_t\|_1 < M,$$

and

$$\|\mathbf{R}_t \cdot \mathbf{I}_t - \mathbf{S}\|_2^2 < M.$$

Note that $\mathbf{I}_t \geq \mathbf{S}$ and \mathbf{S} is the observed image which can be seen as constant matrix on every pixel, we have

$$\begin{aligned}\|\mathbf{R}_t\|_2 &= \left\| \mathbf{R}_t - \frac{\mathbf{S}}{\mathbf{I}_t} + \frac{\mathbf{S}}{\mathbf{I}_t} \right\|_2 \\ &= \left\| \frac{1}{\mathbf{I}_t} \cdot (\mathbf{R}_t \cdot \mathbf{I}_t - \mathbf{S} + \mathbf{S}) \right\|_2 \\ &\leq \left\| \frac{1}{\mathbf{S}} \cdot (\mathbf{R}_t \cdot \mathbf{I}_t - \mathbf{S} + \mathbf{S}) \right\|_2 \\ &\leq \left\| \frac{1}{\mathbf{S}} \right\|_2 \{ \|(\mathbf{R}_t \cdot \mathbf{I}_t - \mathbf{S})\|_2 + \|\mathbf{S}\|_2 \},\end{aligned}$$

where $\frac{1}{\mathbf{I}_t}$ and $\frac{1}{\mathbf{S}}$ is defined as the reciprocal of each element in \mathbf{I}_t and \mathbf{S} , $\frac{1}{\mathbf{S}}$ is performed element-wise.

Because $\mathbf{S} \in L^\infty(\Omega)$ and \mathbf{S} is actually not equal to 0 as described before, both $\left\| \frac{1}{\mathbf{S}} \right\|_2$ and $\|\mathbf{S}\|_2$ are finite. Meanwhile $\|\mathbf{R}_t \cdot \mathbf{I}_t - \mathbf{S}\|_2^2 \leq M$, we can deduce that $\{\mathbf{R}_t\}$ is uniformly bounded in $L^2(\Omega)$, as well as in $L^1(\Omega)$. Combining with $\beta \|\nabla \mathbf{R}_t\|_1 \leq M$, we have $\{\mathbf{R}_t\}$ is uniformly bounded in $BV(\Omega)$. Therefore, there exists an $\mathbf{R}_* \in BV(\Omega)$ such that, up to a subsequence,

$$\mathbf{R}_t \xrightarrow[L^1(\Omega)]{} \mathbf{R}_* \text{ and } \mathbf{R}_t \rightharpoonup \mathbf{R}_* \in L^2(\Omega). \quad (\text{A-3})$$

Note that (A-2) holds for \mathbf{I}_t , which corresponds to \mathbf{R}_t ; therefore, we conclude that, up to a subsequence, $\{(\mathbf{R}_t, \mathbf{I}_t)\}$ satisfies both (A-2) and (A-3). As a consequence of the lower semicontinuity for the $W^{1,2}(\Omega)$ norm, that is,

$$\liminf_{t \rightarrow \infty} (\alpha \|\nabla \mathbf{I}_t\|_2^2 + \gamma \|\mathbf{I}_t - I_0\|_2^2) \geq \alpha \|\nabla \mathbf{I}_*\|_2^2 + \gamma \|\mathbf{I}_* - I_0\|_2^2.$$

Since $\mathbf{R}_t \cdot \mathbf{I}_t \rightarrow \mathbf{R}_* \cdot \mathbf{I}_*$ in $L^2(\Omega)$ and recalling the lower semicontinuity for the $L^2(\Omega)$ norm, we have

$$\liminf_{t \rightarrow \infty} \|\mathbf{R}_t \cdot \mathbf{I}_t - \mathbf{S}\|_2^2 \geq \|\mathbf{R}_* \cdot \mathbf{I}_* - \mathbf{S}\|_2^2.$$

Noting the lower semicontinuity of $BV(\Omega)$ norm that

$$\liminf_{t \rightarrow \infty} \beta \|\nabla \mathbf{R}_t\|_1 \geq \beta \|\nabla \mathbf{R}_*\|_1,$$

we have

$$\min_{(\mathbf{R}, \mathbf{I}) \in \Lambda} E(\mathbf{R}, \mathbf{I}) = \liminf_{t \rightarrow \infty} E(\mathbf{R}_t, \mathbf{I}_t) \geq E(\mathbf{R}_*, \mathbf{I}_*),$$

and $\mathbf{I}_* \geq \mathbf{S}$. The proof is completed.

REFERENCES

- [1] E. H. Land and J. J. McCann, "Lightness and Retinex theory," *J. Opt. Soc. Amer.*, vol. 61, no. 1, pp. 1–11, 1971.
- [2] Z.-U. Rahman, D. J. Jobson, and G. A. Woodell, "Retinex processing for automatic image enhancement," *J. Electron. Imag.*, vol. 13, no. 1, pp. 100–110, 2004.
- [3] D. J. Jobson, Z.-U. Rahman, and G. A. Woodell, "Properties and performance of a center/surround Retinex," *IEEE Trans. Image Process.*, vol. 6, no. 3, pp. 451–462, Mar. 1997.
- [4] Y.-O. Nam, D.-Y. Choi, and B. C. Song, "Power-constrained contrast enhancement algorithm using multiscale Retinex for OLED display," *IEEE Trans. Image Process.*, vol. 23, no. 8, pp. 3308–3320, Aug. 2014.
- [5] S. Wang, J. Zheng, H.-M. Hu, and B. Li, "Naturalness preserved enhancement algorithm for non-uniform illumination images," *IEEE Trans. Image Process.*, vol. 22, no. 9, pp. 3538–3548, Sep. 2013.
- [6] H. Ahn, B. Keum, D. Kim, and H. S. Lee, "Adaptive local tone mapping based on Retinex for high dynamic range images," in *Proc. IEEE Int. Conf. Consum. Electron.*, Jan. 2013, pp. 153–156.
- [7] B. Gu, W. Li, M. Zhu, and M. Wang, "Local edge-preserving multiscale decomposition for high dynamic range image tone mapping," *IEEE Trans. Image Process.*, vol. 22, no. 1, pp. 70–79, Jan. 2013.
- [8] L. Meylan and S. Susstrunk, "High dynamic range image rendering with a Retinex-based adaptive filter," *IEEE Trans. Image Process.*, vol. 15, no. 9, pp. 2820–2830, Sep. 2006.
- [9] S. Pan, X. An, and H. He, "Adapting iterative Retinex computation for high-dynamic-range tone mapping," *J. Electron. Imag.*, vol. 22, no. 2, pp. 023006-1–023006-10, 2013.
- [10] B. J. Lee and B. C. Song, "Local tone mapping using sub-band decomposed multi-scale Retinex for high dynamic range images," in *Proc. IEEE Int. Conf. Consum. Electron.*, Jan. 2014, pp. 125–128.
- [11] X. Lan, H. Shen, L. Zhang, and Q. Yuan, "A spatially adaptive Retinex variational model for the uneven intensity correction of remote sensing images," *Signal Process.*, vol. 101, pp. 19–34, Aug. 2014.
- [12] C. Li, F. Li, C.-Y. Kao, and C. Xu, "Image segmentation with simultaneous illumination and reflectance estimation: An energy minimization approach," in *Proc. IEEE 12th Int. Conf. Comput. Vis.*, Kyoto, Japan, Sep./Oct. 2009, pp. 702–708.
- [13] Y. Liu, R. R. Martin, L. de Dominicis, and B. Li, "Using Retinex for point selection in 3D shape registration," *Pattern Recognit.*, vol. 47, no. 6, pp. 2126–2142, 2014.
- [14] C. Jung, T. Sun, and L. Jiao, "Eye detection under varying illumination using the Retinex theory," *Neurocomputing*, vol. 113, pp. 130–137, Aug. 2013.
- [15] E. H. Land, "The Retinex," *Amer. Sci.*, vol. 52, no. 2, pp. 247–253 and 255–264, 1964.
- [16] E. H. Land, "The Retinex theory of color vision," *Sci. Amer.*, vol. 237, no. 6, pp. 108–128, Dec. 1977.
- [17] E. Provenzi, L. De Carli, A. Rizzi, and D. Marini, "Mathematical definition and analysis of the Retinex algorithm," *J. Opt. Soc. Amer. A*, vol. 22, no. 12, pp. 2613–2621, 2005.
- [18] E. H. Land, "Recent advances in Retinex theory and some implications for cortical computations: Color vision and the natural image," *Proc. Nat. Acad. Sci.*, vol. 80, no. 16, pp. 5163–5169, 1983.
- [19] E. H. Land, "Recent advances in Retinex theory," *Vis. Res.*, vol. 26, no. 1, pp. 7–21, 1986.
- [20] J. McCann, "Lessons learned from mondrians applied to real images and color gamuts," in *Proc. IS&T SID 7th Color Imag. Conf.*, 1999, pp. 1–8.
- [21] B. Funt, F. Ciurea, and J. McCann, "Retinex in MATLAB," *J. Electron. Imag.*, vol. 13, no. 1, pp. 48–57, 2004.
- [22] B. K. P. Horn, "Determining lightness from an image," *Comput. Graph. Image Process.*, vol. 3, no. 4, pp. 277–299, 1974.
- [23] A. Hurlbert, "Formal connections between lightness algorithms," *J. Opt. Soc. Amer. A*, vol. 3, no. 10, pp. 1684–1693, 1986.
- [24] J. M. Morel, A. B. Petro, and C. Sbert, "A PDE formalization of Retinex theory," *IEEE Trans. Image Process.*, vol. 19, no. 11, pp. 2825–2837, Nov. 2010.
- [25] A. Blake, "Boundary conditions for lightness computation in Mondrian world," *Comput. Vis., Graph., Image Process.*, vol. 32, no. 3, pp. 314–327, 1985.
- [26] D. Terzopoulos, "Image analysis using multigrid relaxation methods," *IEEE Trans. Pattern Anal. Mach. Intell.*, vol. 8, no. 2, pp. 129–139, Mar. 1986.
- [27] B. V. Funt, M. S. Drew, and M. Brockington, "Recovering shading from color images," in *Proc. 2nd Eur. Conf. Comput. Vis.*, 1992, pp. 124–132.
- [28] D. J. Jobson, Z.-U. Rahman, and G. A. Woodell, "A multiscale Retinex for bridging the gap between color images and the human observation of scenes," *IEEE Trans. Image Process.*, vol. 6, no. 7, pp. 965–976, Jul. 1997.
- [29] R. Kimmel, M. Elad, D. Shaked, R. Keshet, and I. Sobel, "A variational framework for Retinex," *Int. J. Comput. Vis.*, vol. 52, no. 1, pp. 7–23, 2003.
- [30] M. K. Ng and W. Wang, "A total variation model for Retinex," *SIAM J. Imag. Sci.*, vol. 4, no. 1, pp. 345–365, 2011.
- [31] W. Wang and M. K. Ng, "A nonlocal total variation model for image decomposition: Illumination and reflectance," *Numer. Math., Theory, Methods, Appl.*, vol. 7, no. 3, pp. 334–355, 2014.
- [32] D. Zosso, G. Tran, and S. Osher, "A unifying Retinex model based on non-local differential operators," *Proc. SPIE, Comput. Imag. XI*, pp. 865702-1–865702-16, Feb. 2013.
- [33] D. Zosso, G. Tran, and S. J. Osher, "Non-local Retinex—A unifying framework and beyond," *SIAM J. Imag. Sci.*, vol. 8, no. 2, pp. 787–826, 2015.

- [34] M. Bertalmío, V. Caselles, and E. Provenzi, "Issues about Retinex theory and contrast enhancement," *Int. J. Comput. Vis.*, vol. 83, no. 1, pp. 101–119, 2009.
- [35] R. Palma-Amestoy, E. Provenzi, M. Bertalmío, and V. Caselles, "A perceptually inspired variational framework for color enhancement," *IEEE Trans. Pattern Anal. Mach. Intell.*, vol. 31, no. 3, pp. 458–474, Mar. 2009.
- [36] M. Bertalmío, V. Caselles, E. Provenzi, and A. Rizzi, "Perceptual color correction through variational techniques," *IEEE Trans. Image Process.*, vol. 16, no. 4, pp. 1058–1072, Apr. 2007.
- [37] L. Wang, L. Xiao, H. Liu, and Z. Wei, "Variational Bayesian method for Retinex," *IEEE Trans. Image Process.*, vol. 23, no. 8, pp. 3381–3396, Aug. 2014.
- [38] W. F. Schreiber, *Fundamentals of Electronic Imaging Systems*. Berlin, Germany: Springer-Verlag, 1986.
- [39] T. Goldstein and S. Osher, "The split Bregman method for L1-regularized problems," *SIAM J. Imag. Sci.*, vol. 2, no. 2, pp. 323–343, 2009.
- [40] S. Osher, M. Burger, D. Goldfarb, J. Xu, and W. Yin, "An iterative regularization method for total variation-based image restoration," *Multiscale Model. Simul.*, vol. 4, no. 2, pp. 460–489, 2005.
- [41] R. Hummel, "Image enhancement by histogram transformation," *Comput. Graph. Image Process.*, vol. 6, no. 2, pp. 184–195, 1977.
- [42] P. Getreuer, "Automatic color enhancement (ACE) and its fast implementation," *Imag. Process. Line*, vol. 2, pp. 266–277, Nov. 2012.
- [43] A. A. Michelson, *Studies in Optics*. Chicago, IL, USA: Chicago Univ. Press, 1995.
- [44] A. Mittal, R. Soundararajan, and A. C. Bovik, "Making a 'completely blind' image quality analyzer," *IEEE Signal Process. Lett.*, vol. 20, no. 3, pp. 209–212, Mar. 2013.
- [45] X. Zhang and B. A. Wandell, "A spatial extension of CIELAB for digital color image reproduction," in *SID Int. Symp. Dig. Tech. Papers*, vol. 27, 1996, pp. 731–734.



Xueyang Fu received the M.S. degree in electronics and communication engineering from Xiamen University, Xiamen, China, in 2014, where he is currently pursuing the Ph.D. degree. His current research interests focus on image processing and machine learning.



Yinghao Liao received the B.S. and M.S. degrees in electronics engineering from Xiamen University, China, in 1982 and 1988, respectively.

He is currently an Associate Professor with the School of Information Science and Engineering, Xiamen University. His research interests include image processing, sparse signal representation, and machine learning.



Delu Zeng received the B.S. and M.S. degrees in applied mathematics and the Ph.D. degree in electronic and information engineering from the South China University of Technology, Guangzhou, China, in 2003, 2005, and 2009, respectively.

He is currently an Associate Professor with the School of Information Science and Engineering, Xiamen University, China. His research interests include partial differential equations, machine learning, and their applications in image/video processing, i.e., image segmentation and object tracking.



Yue Huang received the B.S. degree from the Department of Electrical Engineering, Xiamen University, China, in 2005, and the Ph.D. degrees from the Department of Biomedical Engineering, Tsinghua University, Beijing, China, in 2010.

She is currently an Associate Professor with the School of Information Science and Engineering, Xiamen University. Her main research interests include sparse signal representation, and machine learning. Her main research interests include image processing, sparse signal representation, and machine learning.



Xiao-Ping Zhang (M'97–SM'02) received the B.S. and Ph.D. degrees in electronics engineering from Tsinghua University, in 1992 and 1996, respectively, and the M.B.A. (Hons.) degree in finance, economics and entrepreneurship from the University of Chicago Booth School of Business, Chicago, IL.

He has been with the Department of Electrical and Computer Engineering, Ryerson University since 2000, where he is currently a Professor and the Director of the Communication and Signal Processing Applications Laboratory. He has served as the Program Director of Graduate Studies. He is cross appointed to the Finance Department with the Ted Rogers School of Management, Ryerson University. His research interests include image and multimedia content analysis, statistical signal processing, sensor networks and electronic systems, computational intelligence, and applications in big data, finance, and marketing. He is a Frequent Consultant for biotech companies and investment firms. He is the Co-Founder and CEO of EidoSearch, an Ontario-based company offering a content-based search and analysis engine for financial data.

Dr. Zhang is a Registered Professional Engineer in Ontario, Canada, and a member of the Beta Gamma Sigma Honor Society. He is the General Chair of MMSP'15. He was the Publicity Chair of ICME'06 and the Program Chair of ICIC'05 and ICIC'10. He served as a Guest Editor of *Multimedia Tools and Applications*, and the *International Journal of Semantic Computing*. He is a Tutorial Speaker in ACMMM2011, ISCAS2013, ICIP2013, and ICASSP2014. He is an Associate Editor of the IEEE TRANSACTIONS ON SIGNAL PROCESSING, the IEEE TRANSACTIONS ON IMAGE PROCESSING, the IEEE TRANSACTIONS ON MULTIMEDIA, the IEEE TRANSACTIONS ON CIRCUITS AND SYSTEMS FOR VIDEO TECHNOLOGY, the IEEE SIGNAL PROCESSING LETTERS and the *Journal of Multimedia*.



Xinghao Ding was born in Hefei, China, in 1977. He received the B.S. and Ph.D. degrees from the Department of Precision Instruments, Hefei University of Technology, Hefei, in 1998 and 2003, respectively.

He was a Post-Doctoral Researcher with the Department of Electrical and Computer Engineering, Duke University, Durham, NC, USA, from 2009 to 2011. Since 2011, he has been a Professor with the School of Information Science and Engineering, Xiamen University, Xiamen, China. His main research interests include image processing, sparse signal representation, and machine learning.

research interests include image processing, sparse signal representation, and machine learning.